Volume 6
Number 22
21 November 2025
Pages 8195–8726

Materials Advances

rsc.li/materials-advances

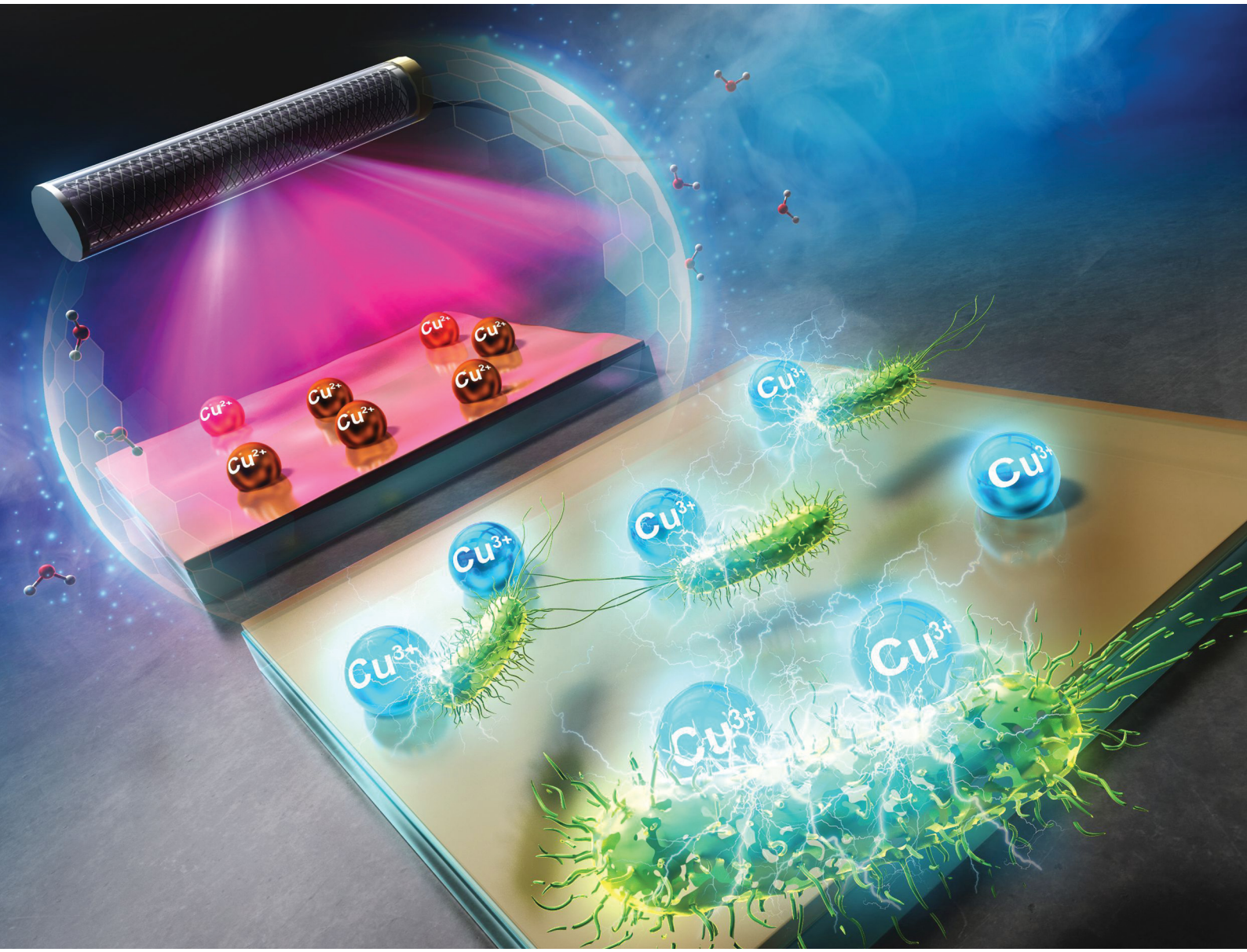

ISSN 2633-5409

ROYAL SOCIETY OF CHEMISTRY

PAPER

Hsiang-Jung Wu *et al.*

Super-rapid bacterial inactivation by Cu^{3+}-ion-dominant films formed *via* UV irradiation of Cu^{2+} complex precursor films with amine ligands

Materials Advances

ROYAL SOCIETY OF CHEMISTRY

PAPER

View Article Online
View Journal | View Issue

Cite this: *Mater. Adv.*, 2025, 6, 8370

Super-rapid bacterial inactivation by Cu^{3+}-ion-dominant films formed *via* UV irradiation of Cu^{2+} complex precursor films with amine ligands

Hsiang-Jung Wu, [ab] Takashi Douura,[a] Shota Takamiya,[a] Koji Yoshikawa,[a] Kenjiro Sugiyama,[c] Mitsunobu Sato[b] and Hiroki Nagai *[b]

Cupryl ion (Cu^{3+})-dominant thin films were easily obtained by UV irradiation of precursor films consisting of Cu^{2+} complexes deposited on a Na-free glass plate, without requiring heat treatment. Transparent thin films, with thicknesses ranging from 0.55 to 0.72 μm, were formed under low humidity conditions (relative humidity below 45%) during UV irradiation. The copper ion valence states and crystalline structures of the thin films were determined using X-ray photoelectron spectroscopy and X-ray diffraction, respectively. Thin films formed at low humidity achieved >99.99% inactivation of *Escherichia coli* within 20 min of inoculation in phosphate buffered saline (PBS). In contrast, thin films formed at higher humidity levels (relative humidity above 50%) showed no significant bacterial inactivation under the same conditions. The concentration of copper ions eluted from the thin films formed under low humidity into the culture medium exceeded 0.74 ppm within 20 min, at least twice the levels observed in films produced under higher humidity conditions. Furthermore, the electron spin resonance spectrum of a solution obtained by immersing the thin films in PBS containing a spin-trapping agent demonstrated the generation of $OH^{\bullet}$ radicals. These findings suggest that the super-rapid bacterial inactivation is primarily attributed to the elution of Cu^{3+} ions from the thin films. The development of easy-to-handle solids involving Cu^{3+} ions, capable of rapidly generating $OH^{\bullet}$ radicals, presents significant potential for applications in public health and water purification.

Received 10th April 2025,
Accepted 18th August 2025

DOI: 10.1039/d5ma00347d

rsc.li/materials-advances

1. Introduction

Many studies have demonstrated the excellent bacterial inactivation capabilities of Cu, copper alloy, Cu_2O, and CuO against *Escherichia coli* (*E. coli*),[1,2] *Staphylococcus aureus* (*S. aureus*),[2,3] *Candida albicans* (*C. albicans*),[4] and *Methicillin-resistant Staphylococcus aureus* (*MRSA*).[2] Recently, we reported the facile formation of polycrystalline Cu_2O thin films by ultraviolet (UV) light irradiation of a precursor film containing a Cu^{2+} complex with amine ligands at room temperature and relative humidity of 60%.[5] The advantage of being able to easily form such thin films is due to a wet-coating technique known as the molecular precursor method, which utilizes the photodecomposition reaction of metal complexes by UV light irradiation.[5] Importantly, a Cu_2O thin film with low crystallinity exhibited exceptional inactivation of SARS-CoV-2 (COVID-19), eliminating over 99.99% of the virus after 1 h of inoculation in Dulbecco's medium (DMEM) on its surface. In contrast, a heat-treated, highly crystallized Cu_2O thin film derived from an identical precursor film showed negligible virus inactivation capability, even after 3 h under identical inoculation.[6] Quantitative analysis of Cu ion elution into the cultivation medium revealed that the crystallinity of thin films plays a critical role in controlling virus inactivation, although the specific valence states of Cu ions were not identified.

Motivated by the effective capability of the above-mentioned antiviral materials and some recent reports on antibacterial materials,[7–11] we further investigated the antibacterial properties of the Cu_2O thin films formed using ultraviolet (UV)-light irradiation. However, preliminary results with *E. coli* in phosphate-buffered saline (PBS) indicated that the Cu_2O thin films, which showed significant antiviral effects, were ineffective within the same inoculation time. Since eluted copper ions are assumed to dominate these activities, it was estimated that the amount of copper ions eluted into PBS during the antibacterial test was lower than that eluted from DMEM during antiviral tests. Such medium-dependent behavior has been reported previously by Behzadinasab *et al.* for commercially

[a] *Research and Development Department, Seiwa Electric MFG Co. Ltd, Joyo, Kyoto 6100192, Japan*
[b] *Department of Applied Physics, Kogakuin University of Technology and Engineering, Hachioji, Tokyo 1920015, Japan. E-mail: nagai@cc.kogakuin.ac.jp*
[c] *Department of Applied Chemistry, Kogakuin University of Technology and Engineering, Hachioji, Tokyo 1920015, Japan*

available Cu_2O particles.[12] To increase the amount of copper eluted into PBS, we investigated several film formation conditions to reliably reduce the crystallinity of the copper oxide. It was found that even with the same UV light intensity and irradiation time at room temperature, a threshold relative humidity exists, beyond which the product undergoes significant changes.

In this study, we report a method for producing a thin film material with super-rapid bacteria-inactivation capability in PBS using a simple UV-light irradiation process under low-humidity conditions. To characterize the formed films, X-ray diffractometer (XRD), scanning electron microscopy (SEM), atomic force microscopy (AFM), stylus profilometer, X-ray photoelectron spectroscopy (XPS), Fourier-transform infrared (FT-IR) spectra, flame atomic absorption spectrometry (FAAS), and electron spin resonance (ESR) spectroscopy were used.

2. Experimental

2.1. Used reagents and substrate

Ethanol, propylamine, ethylenediamine, Cu standard solution (1000 ppm), and nitric acid were purchased from Nacalai Tesque, Inc. (Kyoto, Japan). Copper(II) formate tetrahydrate (98%) and the spin-trapping agents 5,5-dimethyl-1-pyrroline-*N*-oxide (DMPO), disodium dihydrogen phosphate (Na_2HPO_4), and potassium dihydrogen phosphate (KH_2PO_4) were purchased from FUJIFILM Wako Pure Chemical Corporation (Osaka, Japan). A copper standard solution with a Cu ion concentration of 1.001 g L^{-1} in 0.1 mol L^{-1} nitric acid was purchased from Kanto Chemical Co., Inc. (Tokyo, Japan). Deionized water with a resistivity over 18 MΩ cm was purified using an Arium Pro VF (SARTORIUS, Goettingen, Germany). All reagents were of analytical grade and were used without further purification. PBS was prepared by dissolving 5.70 g of Na_2HPO_4 and 3.65 g of KH_2PO_4 in 1000 mL of water. PBS was used as the medium for bacterial inactivation tests and various analyses. Na-free glass plates measuring 30 × 30 mm^2 with a thickness of 1.1 mm were purchased from Corning Inc. (New York, NY, USA). The substrates were cleaned using an ozone cleaner to remove organic contaminants and subsequently dried in an oven at 70 °C before coating.

2.2. Solution preparation and coating method

The precursor solution containing the Cu^{2+} complex of propylamine and ethylenediamine was prepared as described in a previous study.[5] The Cu^{2+} concentration in the solution was 1.0 mmol g^{-1}. A volume of 130 μL of the precursor solution was dropped onto the Na-free glass plate using a micropipette and spin-coated using a two-step process (1st step: 1000 rpm for 5 s; 2nd step: 2000 rpm for 30 s). The coated plate was dried in a drying oven at 70 °C under 9% humidity for 24 h, yielding the precursor film, denoted as **PRE**.

2.3. UV irradiation of Cu^{2+} complex film under controlled humidity

The precursor film (**PRE**) was subjected to UV irradiation using a germicidal lamp (Coospider, Jinyun, China) for 4 h in a chamber maintained at 30 °C with controlled humidity levels (35–60%). The light intensity at 254 nm, monitored using an illuminator (UIT-250, Ushio, Tokyo, Japan), was 8.0 mW cm^{-2}. The UV-irradiated films were denoted as **FX** (X; controlled relative humidity = 35, 40, 45, 50, and 60%). Additionally, the UV-irradiated film at 40% humidity (**F40**) was heat-treated at 250 °C for 15 min under 1 L min^{-1} of N_2 (purity 99.999%, Kyoto Teisan, Kyoto, Japan) flow. This heat-treated film was denoted as **F40H**.

2.4. Characterization

The crystallized components in **FX** and **F40H** were analyzed using an XRD (SmartLab, Rigaku, Tokyo, Japan) with Cu Kα radiation operating at 30 kV and 5 mA. Measurements were conducted using parallel beam optics at an incidence angle of 0.3°, scanning continuously in the 2θ range from 10 to 60° at a step width of 0.1° and a scanning speed of 4° per min. The XRD pattern of the dried precursor film **PRE** was also measured.

The surface morphologies of **FX** and **F40H** were observed using SEM (JSM-6010LA, JEOL, Akishima, Japan). The accelerating voltage for sample observation was 15 kV. Before observation, all the samples were coated with Pt using a sputtering coater for 20 s to improve the electrical conductivity of the sample surface. The surface roughness of **FX** and **F40H** was determined using AFM (OLS4500, Olympus, Tokyo, Japan). The film thicknesses of **FX** and **F40H** were measured using an XP-1 module stylus profilometer (AMBios Technology, California, USA). The stylus load used for the measurement was 1.0 mg, and the measurement rate was 0.2 mm s^{-1}. The adhesion strengths of **F40** and **F40H** between the film and the substrate were evaluated using a tensile test. The pins for tensile testing were connected by a resin between the pin and the film surface and heat-treated at 150 °C for 1 h. The pulling forces of the pins ranged from 26.5 to 107.9 N.

The chemical compositions of **PRE**, **FX**, and **F40H** were analyzed by XPS (XP, ESCA5700, ULVAC-PHI Inc., Japan), with an Al Kα X-ray (1486.6 eV) source generated at 15 kV and 27 mA. The chemical shifts of C 1s, O 1s, N 1s, and Cu $2p_{3/2}$ were calibrated by setting the center of the C–C peak at 284.6 eV. A resolution of 0.1 eV was used for each measurement. The thin films were analyzed without Ar^+ etching. Curve fitting was performed using OriginPro 2023 software (Lightstone Corp., Tokyo, Japan) with a Voigt function and a χ^2 tolerance value of 1×10^{-9}.

FT-IR spectra of **PRE**, **FX**, and **F40H** were measured using an FT-IR spectrometer (FT-IR-4600, JASCO, Tokyo, Japan) in the range of 4000–500 cm^{-1} using the attenuated total reflection (ATR) method, with 100 cumulative scans.

The amount of copper ions eluted from **FX** and **F40H** into PBS after 20 min of immersion was analyzed using FAAS (AA-7000, Shimadzu, Kyoto, Japan). The copper ion concentration in each sample was determined from the average of three measurements. A calibration curve for copper ion detection in the range from 0.7 to 5.0 ppm was obtained using diluted copper standard solutions in 0.1 mol L^{-1} nitric acid.

Bacterial inactivation tests of **FX** and **F40H** were performed according to the Japan Industrial Standard (JIS) Z 2801, which

was also developed as the International Organization for Standardization (ISO) 22196. *E. coli* was used as the test bacterium. The bacterial inactivation capability of each sample was calculated as the average value of three experiments. The bacterial inactivation capability was represented by the reduction value (R) and reduction rate (R%), defined by eqn (1) and (2), respectively.

$$R = (\log C_t - \log C_0) - (\log F_t - \log F_0) \quad (1)$$

$$R\% = (1 - 10^{1/R}) \times 100\% \quad (2)$$

In these equations, $\log C_0$ and $\log C_t$ represent the number of bacteria on the glass surface immediately after inoculation and after t min of inoculation, respectively, and $\log F_0$ and $\log F_t$ correspond to the bacterial counts on the film surface under the same conditions.

The ESR spectrum of a solution obtained by immersing **F40** (stored under ambient conditions for 2 months) in PBS containing DMPO as a spin-trapping agent was measured. A solution of PBS containing 5% (w/v) DMPO was prepared, and 100 μL was applied to **F40** *via* pipetting. Then, 50 μL of this solution was added to a capillary tube (LCT-50; LABOTEC Co., Ltd Tokyo, Japan) for ESR analysis using an ESR spectrometer (JES-FA-100; JEOL, Tokyo, Japan). Conditions included a microwave power of 4 mW, a sweep width of 7.5 mT, a modulation width of 0.2 mT, an amplitude of 300, a sweep time of 4 min, and a time constant of 0.3 s. PBS without the film was analyzed as a reference. An Mn/MgO sample served as an external signal marker.

3. Results

3.1 Crystal structure of the thin films and precursor film

Fig. 1(a) shows the XRD patterns of **PRE**, **FX**, and **F40H**. No clear peak was observed for **PRE**. The two peaks at 36.6°–37.0° and 42.7° observed for **FX** and **F40H** correspond to the (111) and (200) crystal phases of Cu_2O, respectively. In addition, a broad peak at 29.8° corresponding to the (110) crystal phase of Cu_2O was observed for **F60** and **F40H**. Fig. 1(b) shows the peak areas and FWHM of the Cu_2O(111) phase in **FX** and **F40H**. The peak area was obtained as the integrated area using the Smart Lab Studio II software installed with the instrument.

3.2. Surface morphology, film thickness, and adhesion strength of thin films

The surface SEM images of **FX** and **F40H** are shown in Fig. 2. Many cracks are clearly observed in the thin film **F35**. The number of cracks decreased drastically with increasing humidity (**F40** and **F45**), and no cracks were observed at humidity levels above 50% (**F50** and **F60**). Notably, **F40H** obtained by heating **F40** at 250 °C has a uniform surface.

The 3D-AFM images of **FX** and **F40H** are shown in Fig. 3. The arithmetic average surface roughness and film thickness values are listed in Table 1. The results of the transmittance spectra and haze ratios of these films were described in Fig. S1 and Table S1, respectively.

The adhesion strength of **F40** and **F40H** to the glass plate was <4.8 MPa and 11.6 MPa, respectively.

3.3. Chemical composition of thin films

The deconvoluted peaks obtained by analyzing the XPS spectra of **PRE**, **FX**, and **F40H** in the ranges of (a) Cu $2p_{3/2}$, (b) Satellite Peak of Cu (c) O 1s, (d) C 1s, and (e) N 1s are shown in Fig. 4. The XPS Cu $2p_{3/2}$ spectra of all films were smoothed using an installed program before deconvolution. The main and satellite peak regions of Cu $2p_{3/2}$ were successfully deconvoluted into three and five components respectively.

Binding energies of 932.9, 933.9, and 935.0 eV in the Cu $2p_{3/2}$ range correspond to the chemical composition of Cu^+, Cu^{2+} ions, and Cu^{3+}, respectively.[13,14] The peak area ratios of Cu^+,

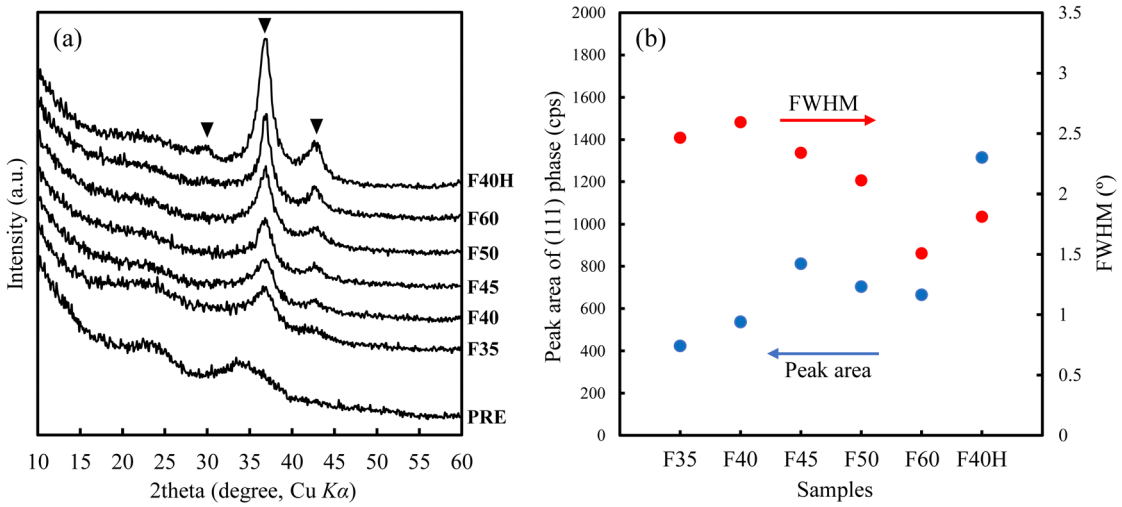

Fig. 1 (a) XRD patterns of the precursor film (**PRE**), UV-irradiated film (**FX**, X = controlled humidity in the range of 35–60%), and **F40H** obtained by heat treatment of **F40**. Triangles (▼) denote the crystal phases of Cu_2O (ICDD card no. 01-078-5772). (b) Peak area and FWHM of the Cu_2O(111) phase in **FX** and **F40H**.

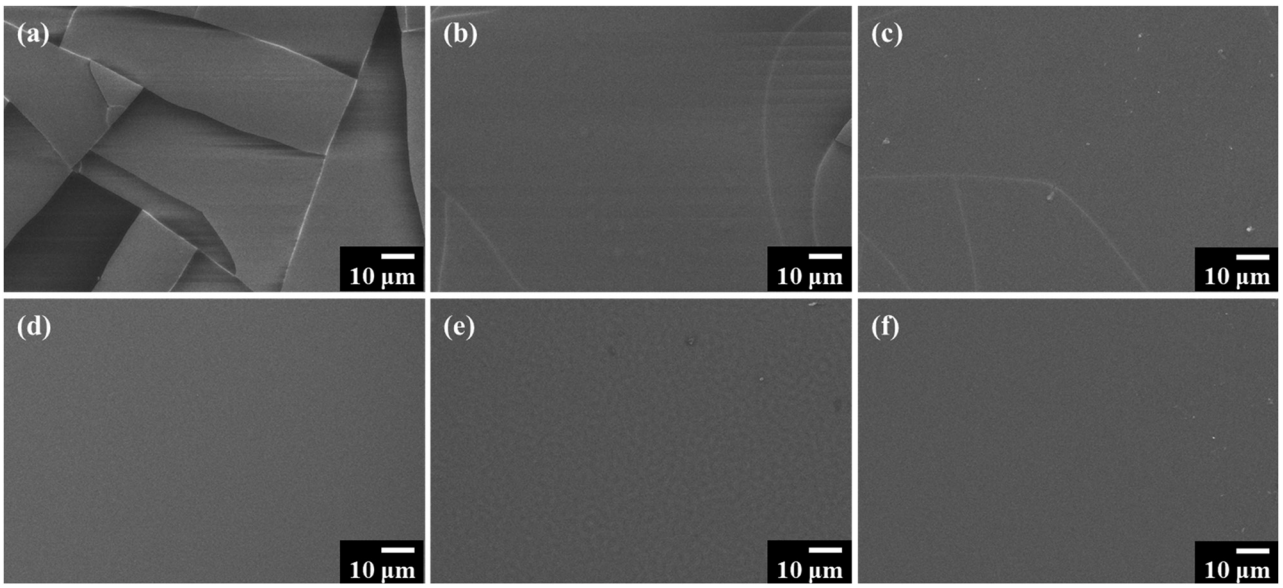

Fig. 2 SEM images of UV-irradiated films: (a) **F35**, (b) **F40**, (c) **F45**, (d) **F50**, (e) **F60**, and (f) **F40H** (obtained by heat treatment of **F40**). All the samples were sputtered with Pt for 20 s to improve surface conductivity before observation.

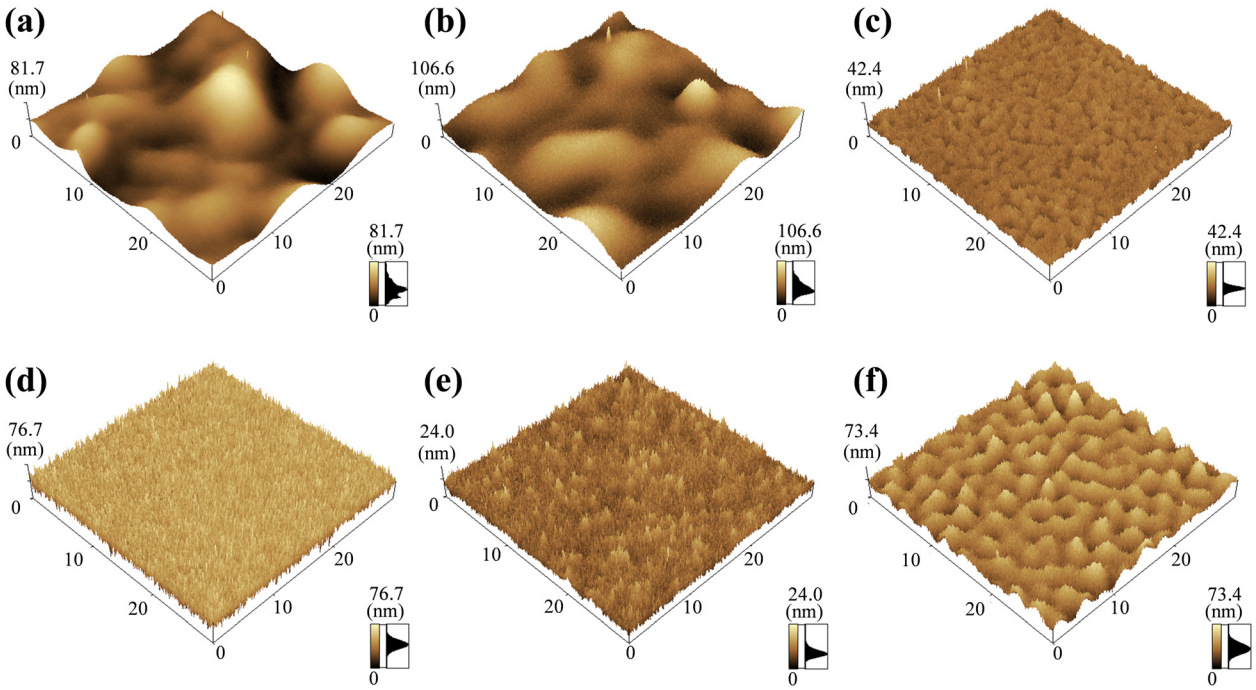

Fig. 3 3D-AFM mapping image of (a) **F35**, (b) **F40**, (c) **F45**, (d) **F50**, (e) **F60**, and (f) **F40H**. Vertical scales differ for each image.

Table 1 Arithmetic average surface roughness (R_a) and film thickness of **PRE**, **FX**, and **F40H**. Roughness was calculated in an arbitrarily selected area of 30 × 30 μm^2

Sample	PRE	F35	F40	F45	F50	F60	F40H
Thickness (μm)	0.89	0.72	0.71	0.55	0.53	0.47	0.23
Roughness (nm)	—	11	12	2	6	7	2

Cu^{2+}, and Cu^{3+} ions in **PRE**, **FX**, and **F40H** are summarized in Fig. 5 and Table S2.

In the satellite peak region of **PRE**, deconvolution yielded only three strong peaks at 940.8, 942.4, and 943.7 eV (S1, S2, and S3 in Fig. 4). It is well known that in XPS analysis of Cu^{2+} materials, the main Cu^{2+} peak appears along with three distinct satellite peaks in the 940–945 eV range.[15,16] Therefore, the deconvoluted peaks S1, S2, and S3 can be due to Cu^{2+} complex.

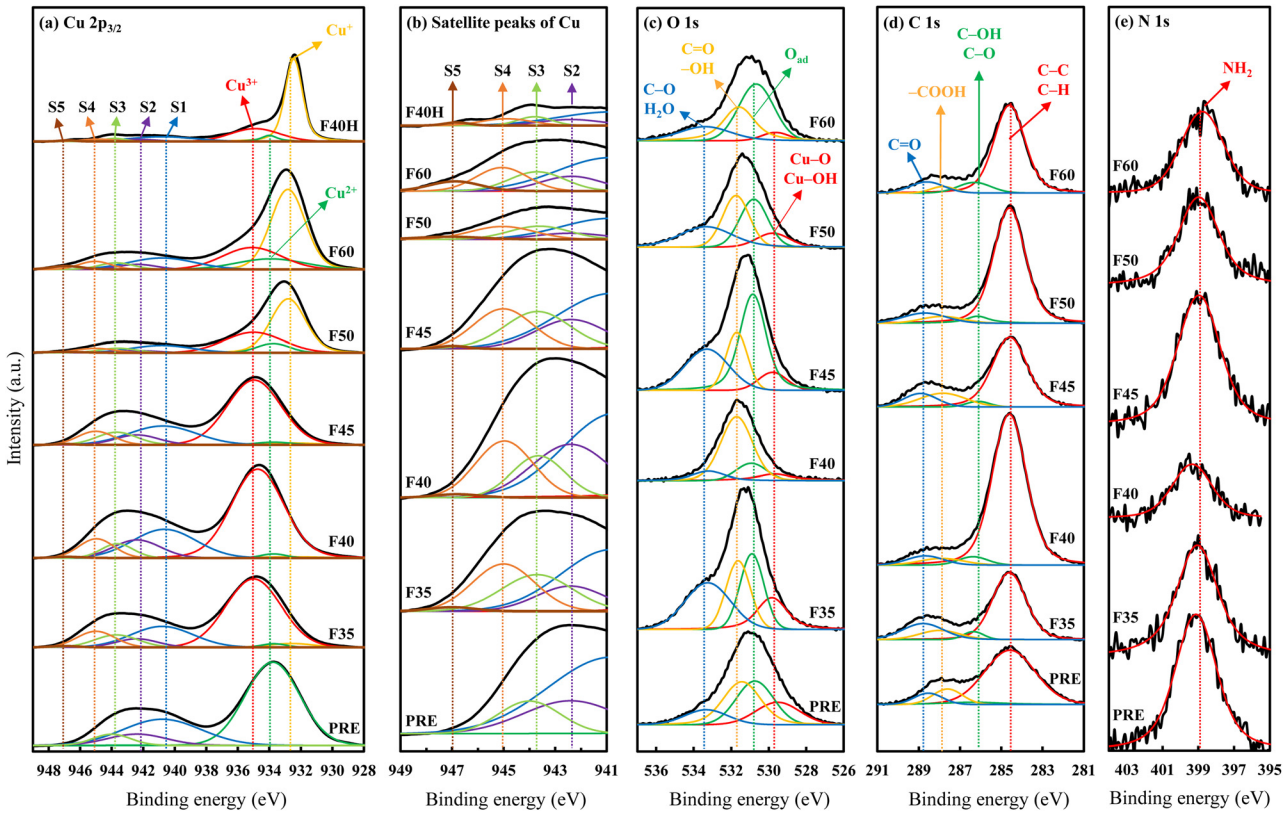

Fig. 4 XPS spectra in the regions of (a) Cu $2p_{3/2}$, (b) satellite peak of Cu, (c) O 1s, (d) C 1s, and (e) N 1s for **PRE**, **FX** (X = controlled humidity = 35–60%), and **F40H**. Colored solid curves indicate theoretically fitted curves based on Voigt distribution, generated using peak-splitting software in OriginPro.

In all cases of the UV-irradiated films **FX** and **F40H**, deconvolution yielded four relatively strong peaks at 940.8, 942.4, 943.7, and 945.0 eV (S1, S2, S3, and S4 in Fig. 4), and one weak peak at 947.0 eV (S5 in Fig. 4). Martin *et al.* reported that the main peak positions for Cu^{+} and Cu^{0} are the same, and Cu^{+} exhibits two fairly weak and broad satellite peaks between 942 and 948 eV, while Cu^{0} demonstrates no corresponding satellite peaks.[15] Thus, the presence of high-energy satellite peaks in the UV-irradiated film indicates that the main peak can be assigned to Cu^{+}.

On the other hand, **F35**, **F40**, and **F45** exhibit one weak peak (S5) and another intense peak (S4) around 947 and 945 eV respectively, in addition to the satellite peaks due to Cu^{2+}. Several research groups reported that the intense satellite peaks around 945 eV can be assigned to those of Cu^{3+} in the synthesized complexes and oxides.[17,18] The weak peak S5 at the highest energy can be assigned to the aforementioned Cu^{+} satellite peak. Therefore, it is suggested that the intense peak S4 is primarily due to Cu^{3+} and overlaps one of the weak Cu^{+} satellite peaks in this region.

In the region of O 1s of **PRE** and **FX**, the peaks observed at 529.7, 530.8, 531.6, and 533.3 eV are assignable to Cu–O, adsorbed oxygen (O_{ad}),[19,20] C═O or hydroxy group,[21–23] and C–O or adsorbed H_2O,[21–23] respectively. In the region of C 1s of **PRE** and **FX**, peaks at 284.6, 286.2, 287.8, and 288.7 eV can be assigned to C–C/C–H,[23,24] C–OH/C–O,[21,23,24] –COOH,[21,24] and C═O,[23] respectively. In the region of N 1s of all films, a hollow peak was observed at 399.4 eV that corresponds to NH_2.[25] The estimated amounts of N atoms are less than 5%, using relative

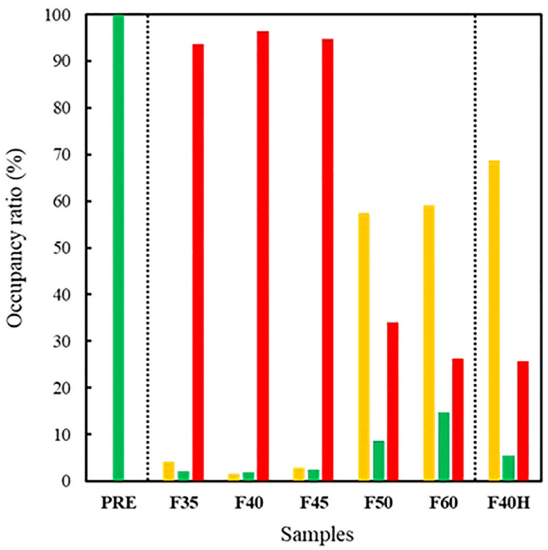

Fig. 5 Occupancy (%) of Cu^{+} (yellow), Cu^{2+} (green), and Cu^{3+} (red) ions, as analyzed from the Cu $2p_{3/2}$ peaks in the XPS spectra of UV-irradiated film (**FX**, X = controlled humidity in the range of 35–60%), and **F40H** (obtained by heat treatment of **F40**).

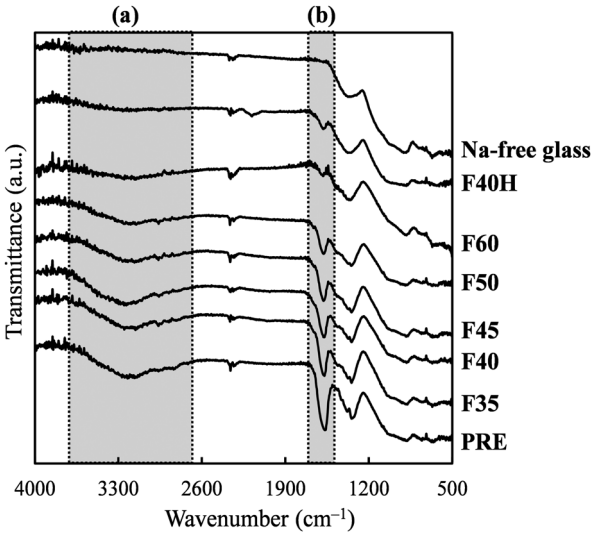

Fig. 6 FT-IR spectra of the precursor film (**PRE**), UV-irradiated film (**FX**, X = controlled humidity = 35–60%), and **F40H** (obtained by heat treatment of **F40**).

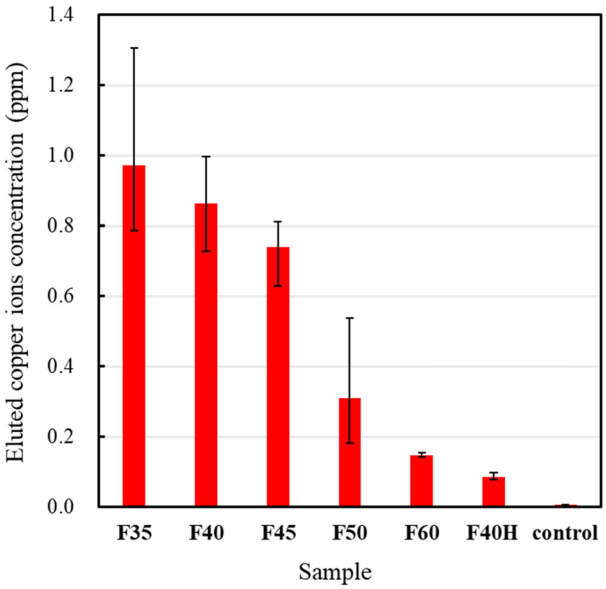

Fig. 7 Eluted copper ion concentration in PBS after 20 min of immersion of **FX** and **F40H**, along with that of PBS before immersion (control).

sensitivity factor of N atom. Therefore, the deconvolution of the N 1s peaks was not performed, owing to the low signal-to-noise ratios of the peaks.

Fig. 6 shows the FT-IR spectra of **PRE**, **FX**, and **F40H** measured using ATR. Region (a), in the range of 3600–2600 cm^{-1} mainly corresponds to the OH stretching[26,27] and CH_3/CH_2 stretching modes.[27,28] Region (b), in the range of 1700–1500 cm^{-1}, contains peaks corresponding to the C–N bending mode and COO^- stretching modes.[26]

3.4. Cu ion elution from the formed thin films

Fig. 7 shows the amounts of Cu ions eluted from **FX** and **F40H** after immersion in PBS for 20 min. The average concentrations of copper ions eluted from **F35**, **F40**, **F45**, **F50**, **F60**, and **F40H** were 0.97, 0.86, 0.74, 0.31, 0.15, and 0.09 ppm, respectively. The Cu ion concentration in PBS (control) was undetectable (less than 0.01 ppm).

3.5. Bacteria inactivation capability of obtained thin films

Table 2 shows the bacterial inactivation capabilities for **FX** and **F40H**. After 20 min of contact with *E. coli*, thin films **F35**, **F40**, and **F45** exhibited reduction values (R) >4.0, demonstrating 99.99% inactivation. However, **F50**, **F60**, and **F40H** exhibited <1.0, indicating negligible bacterial inactivation.

Table 2 Reduction value of UV-irradiated films (**FX**, X = controlled humidity = 35–60%), and **F40H** after heat treatment of **F40**. The evaluation method is based on the JIS Z 2801, which was developed as the standard of ISO 22196. The *E. coli* was used for the inactivation test, and the contact duration was 20 min

Sample	F35	F40	F45	F50	F60	F40H
Reduction value (R)	4.5	4.3	4.5	0.0	0.1	0.9

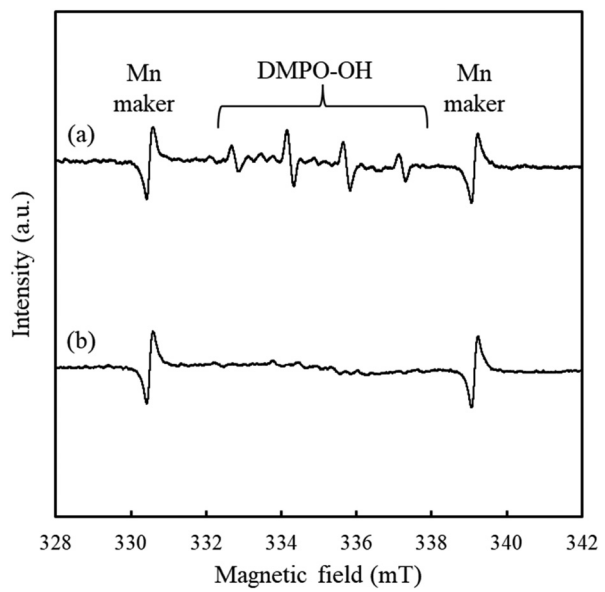

Fig. 8 ESR spectra of (a) DMPO–OH radical observed in an aqueous DMPO solution after immersion of **F40**, and (b) as-prepared DMPO solution without film immersion.

3.6. Detection of radical generation from UV-irradiated thin film

The spectrum of the detected DMPO–OH radicals is shown in Fig. 8(a). In the mid-section, four peaks with relative intensities of 1 : 2 : 2 : 1, which are the characteristic signals of DMPO–OH radicals, were detected in an aqueous solution immersed with **F40** for 20 min, with the two side signals of Mn used as an external reference. No radical signal, except for the Mn reference, was detected in the as-prepared DMPO solution (Fig. 8(b)), indicating the formation of $OH^{\bullet}$ radicals during the immersion of **F40**.

4. Discussion

4.1. Relationship between copper ion elution from UV-irradiation thin films and humidity as a formation condition

The Cu-ion elution behavior of UV-irradiated thin films **FX** during immersion in PBS, as indicated by the AAS results (Fig. 7), varied significantly. This elution behavior depended on the humidity during film conversion by UV irradiation and could be classified into two groups: films with high Cu-ion elution (**F35**, **F40**, and **F45**) and those with low elution (**F50**, **F60**, and **F40H**). In this section, we discuss the elution of Cu ions from UV-irradiated thin films during PBS immersion.

XRD analysis detected Cu_2O crystal peaks in all UV-irradiated films (**FX**), although the intensities and FWHM values varied (Fig. 1). As the humidity of the chamber during UV exposure increased, the peak area of the $Cu_2O(111)$ phase in the XRD pattern of the obtained **FX** also increased, while the FWHM decreased. This trend indicates that the crystallinity of Cu_2O in **FX** improves with an adequate supply of water to the precursor film surface during the photoinduced reaction (Fig. 1(b)).

Furthermore, analysis of the XPS spectra revealed that the UV-irradiated films contained only a small amount of Cu^+ ions when the humidity was below 45% (Fig. 4 and 5). This observation suggests that a sufficient number of water molecules must be available at the film surface to convert the original Cu^{2+} ions into Cu^+ ions, thereby forming Cu_2O crystals. The critical humidity for this photoinduced reaction lies between 45% and 50%, a threshold that aligns perfectly with the two distinct groups categorized by Cu-ion elution.

When a photoinduced reaction occurs in air at humidity levels above the critical humidity, water molecules participate in the reduction of Cu^{2+} ions, sequentially converting them into Cu^+ ions from near the surface of the precursor film to its depths, resulting in the formation of Cu_2O. However, at humidity levels below the critical humidity, an alternative photoinduced reaction occurs, likely producing Cu^{3+} species, which are highly soluble in PBS.

As a result, thin films formed under high humidity conditions exhibited reduced Cu-ion elution; even if a certain amount of Cu^{3+} species was generated at the bottom of the crystallized Cu_2O layer, direct contact between PBS and the Cu^{3+} species was prevented, reducing the amount of copper ions that dissolved. In the case of **F40H**, it is presumed that the thermal reaction of **F40** promoted chemical bonding at the interface between the film and the substrate, thereby doubling the adhesive strength, and also promoted further decomposition of organic residues in the UV-irradiated film, leading to the crystallization of Cu_2O in the film. The concentration of eluted Cu ions was consequently lowest.

In our previous study, we found that the amount of Cu ions eluted from Cu_2O thin films into Dulbecco's modified Eagle's medium (DMEM), used as a culture medium for the COVID-19 virus, varied significantly with the crystallinity of Cu_2O.[6] However, as mentioned in the Introduction, this effect was not replicated against bacteria in PBS, a bacterial culture medium. In this study, by controlling the humidity during film formation by UV irradiation, we successfully produced thin solid films mainly composed of Cu^{3+} species. These films demonstrate enhanced Cu-ion elution in PBS compared to Cu_2O, highlighting their potential for targeted applications.

4.2. Plausible photoinduced reactions in precursor films under different humidity levels

In the above section, we classified the solubility of UV-irradiated films in PBS into two types based on the strong involvement of water molecules, which is significantly influenced by humidity. Furthermore, it is worth considering the photoinduced reaction pathways that lead to the generation of Cu^+ and Cu^{3+} ions *via* the Cu^{2+} complex.

Notably, the film thickness of Cu^{3+}-dominant films was greater than that of Cu^+-dominant films (Table 1). Additionally, the FT-IR spectra of the Cu^{3+}-dominant films showed the retention of carboxy groups, unlike Cu^+-containing films (Fig. 6). These results strongly suggest that a novel Cu^{3+} species forms from the starting Cu^{2+} complexes *via* UV irradiation of precursor films at low humidity. This species is likely stabilized by organic residues and/or counterions, as the organic compositions detected from XPS spectra of C 1s and O 1s. In addition, we measured and analyzed the Raman spectra of the precursor film, UV-irradiated films, and used glass substrate. In each spectrum, a broad band due to the Na-free glass substrate was observed around 480 cm^{-1}. In the spectra of **F45** and **F40H**, two very tiny peaks at 587 and 618 cm^{-1}, respectively assignable to Cu^{3+} component and Cu_2O, were observed[29] (Fig. S2).

Based on these suggestions, the photoinduced reactions described by eqn (3) and (4) are proposed. In these equations, L, n, M, m, and $[L_nM^m]$ represent the ligand, number of ligands, metal, valence of the metal, and the metal complex in its excited state achieved by UV light irradiation, respectively.

$$H_2O + [L_nM^m] \rightarrow HO^{\star} + HL_n + M^{m-1} \quad (3)$$

$$[L_nM^m] + XY \rightarrow L_nM^{m+1}(X)(Y) \quad (4)$$

Eqn (3) and (4) illustrate two typical reactions involving changes in the valence of the central metal in an organometallic complex: reductive elimination and oxidative addition, respectively. Typically, such reactions occur with organic compounds in organic solvents. However, in this context, atmospheric water (H_2O) replaces the usual alkyl compound (RH) in eqn (3), while XY substitutes for conventional reactants such as aryl halide or aldehyde *etc.*[30,31] in eqn (4). The coefficients of the reactions are omitted due to the difficulty in determining reactant concentrations in the solid state.

The surface morphology of the UV-irradiated films **FX** varies depending on the humidity level during formation. At high humidity levels, especially **F50** and **F60**, the preferential formation of Cu^+ ions by the reductive elimination of the ligand according to eqn (3), crystallization to Cu_2O, and subsequent densification as even-surface films, in which Cu^+ ions increased, occurred upon UV irradiation in the presence of atmospheric water (Fig. 3 and Table 1).

On the other hand, when the humidity was low, there were insufficient water molecules to induce the reductive elimination of the ligands, so the irradiated light energy preferentially induced the oxidative addition reaction in the precursor film according to eqn (4). Although the chemical species corresponding to the additional XY in eqn (4) remained unidentified, the presence of formate, a type of aldehyde, suggests its involvement in the oxidative addition reaction.

As a result, **F35** and **F40**, which showed minimal thickness reduction, developed rough surface morphology with partial peeling and cracks. This behavior can be attributed to the preferential formation of Cu^{3+} species through the reaction of residual ligands and counterions (Fig. 2 and 3). For film **F45**, the film thickness reduction and surface morphology were comparable to those at high humidity. However, the Cu^{3+} content was still high and almost identical to that of the thin films formed at low humidity. This finding indicates that a humidity of approximately 45% serves as the threshold where the preference between the two reaction types switches.

Behzadinasab *et al.* previously reported that commercially available Cu_2O particles, likely with high crystallinity, exhibited high solubility in DMEM but negligible solubility in PBS.[12] These results suggest the hypothesis that Cu^{3+} species may elute into PBS. Importantly, UV irradiation of the precursor Cu^{2+} complex film enables two easily tunable, humidity-dependent reactions—reductive elimination and oxidative addition—leading to the formation of Cu^{+} and Cu^{3+} species, respectively.

4.3. Super-rapid bacteria inactivation capability of the UV-irradiated films

The XPS results and bacterial inactivation test indicate that the Cu^{3+}-dominant films exhibit a super-rapid bacterial inactivation capability (Fig. 5 and Table 2). To understand this phenomenon, the ESR results (Fig. 8) provide valuable insights, showing that **F40** generates $OH^{\bullet}$ radicals by dissolving in PBS. Recently, Feng *et al.* focused on the generation of strong oxidizing species of Cu^{3+} ions using the Fenton-like reaction of copper and their application in the degradation of contaminants by Cu^{3+} ions.[32] This research indicates that the Fenton-like reaction can generate Cu^{3+} ions in solution and hydroxyl radicals by the further reaction of the resultant Cu^{3+} ions with OH^{-} ions derived from water. Furthermore, Liu *et al.* reported a Cu^{+}–H_2O_2 Fenton-like reaction that generates Cu^{3+} ions in water-based preparations. This reaction enhances sludge dewaterability, with Cu^{3+} exhibiting strong oxidizing reactivity and efficiently decomposing organics in sludge.[33]

Based on these findings, we propose that Cu^{3+} species, converted from Cu^{2+} ions through oxidative addition reactions, dissolve into PBS during the immersion of the UV-irradiated solid film in the culture medium. These dissolved species generate $OH^{\bullet}$ radicals, which account for the remarkable and rapid bacterial inactivation capability. The $OH^{\bullet}$ radical generation by using the thin solid films of this study includes a process of dissolving the solid, which is different from the recent studies on which the solid surface exhibits antibacterial properties by generation of reactive oxygen species at internal cells after metal ions entering.[8,9]

To investigate the involvement of the aldehyde group of formate in the oxidative addition reaction, we prepared another precursor solution of the Cu^{2+} complex using copper acetate instead of copper formate. A thin film was then formed by UV irradiation onto a spin-coated precursor film at a relative humidity of 40%. The preliminary results indicated that the bacterial inactivation capability of the film was significantly lower than that of **F40**, indicating the importance of the aldehyde group in the counter anion. The details of these results will be reported elsewhere.

Conclusions

This study successfully achieved the facile formation of a Cu^{3+}-dominant thin solid film with high solubility in PBS through UV irradiation of a precursor film involving Cu^{2+} complexes at ambient temperature. It was clarified that to obtain such a thin solid film mainly composed of Cu^{3+} species, the precursor Cu^{2+} complex must be UV-irradiated in an atmosphere with low humidity, specifically below 45%. The Cu^{3+}-dominant thin solid film demonstrated super-rapid bacterial inactivation capability, as evidenced by a standard inoculation test using PBS. The solid material inactivated 99.99% of *E. coli* within 20 min. Furthermore, it was shown that this solid material generates $OH^{\bullet}$ radicals in solution when dissolved in PBS. The rapid inactivation of bacteria was attributed to the strong oxidizing capability of the released Cu^{3+} species. Given its ability to generate $OH^{\bullet}$ radicals when dissolved in PBS, this material holds potential for decomposing organic pollutants, making it a promising candidate for water purification applications. Its effectiveness suggests it could contribute significantly to public health and safety.

To the best of our knowledge, this is the first report of Cu^{3+}-dominant thin films that can be easily formed as stable solids through UV irradiation of a precursor film containing a Cu^{2+} complex in a humidity-controlled atmosphere. In contrast, previous studies have only reported the generation of Cu^{3+} species in the liquid phase.

Author contributions

H-J Wu, T. Douura, and S. Takamiya contributed equally. Hsiang-Jung Wu: writing – original draft, investigation, validation, formal analysis, data curation, visualization. Takashi Douura: conceptualization, project administration, investigation, validation, formal analysis, data curation, visualization, funding acquisition. Shota Takamiya: investigation, validation, formal analysis, data curation, visualization. Koji Yoshikawa: project administration, funding acquisition. Kenjiro Sugiyama: investigation, resources. Mitsunobu Sato: writing – review & editing, supervision. Hiroki Nagai: writing – review & editing, supervision.

Conflicts of interest

There are no conflicts to declare.

Data availability

The authors confirm that the data supporting the findings of this study are available within the article and its SI. See DOI: **https://doi.org/10.1039/d5ma00347d**

Acknowledgements

This study was supported by the international research project of Kogakuin University, and the Japan Science and Technology Agency (JST)-Mirai Program, Grant Number JPMJMI18DA. We are sincerely grateful to Prof. Hiroshi Kawakami for his suggestions on the field of anti-bacterial materials and constructive feedback to improve the readability of this manuscript.

References

1 W. Wu, W. Zhao, Y. Wu, C. Zhou, L. Li, Z. Liu, J. Dong and K. Zhou, *Appl. Surf. Sci.*, 2019, **465**, 279–287.
2 Y. Wang, Q. Wang, G. Wu, H. Xiang, M. T. Innocent, M. Zhai, C. Jia, P. Zou, J. Zhou and M. Zhu, *J. Mater. Sci. Technol.*, 2022, **122**, 1–9.
3 A. Singh, A. Ahmed, K. N. Prasad, S. Khanduja, S. K. Singh, J. K. Srivastava and N. S. Gajbhiye, *Antimicrob. Agents Chemother.*, 2015, **59**(11), 6882–6890.
4 O. Długosz, K. Lis, W. Matyjasik, P. Radomski, J. Pulit-Prociak and M. Banach, *J. Cluster Sci.*, 2022, **34**(4), 2153–2165.
5 H.-J. Wu, N. Tomiyama, H. Nagai and M. Sato, *J. Cryst. Grow.*, 2019, **509**, 112–117.
6 H.-J. Wu, T. Douura, K. Kumagai, H. Nagai, H. Kawakami, E. E. Nakayama, T. Shioda and M. Sato, *Funct. Mater. Lett.*, 2023, **15**, 2251053.
7 P. Kumar, M. C. Mathpal, S. Hamad, S. V. Rao, J. H. Neethling, A. J. van Vuuren, E. G. Njoroge, R. E. Kroon, W. D. Roos and H. C. Swart, *Appl. Mater. Today*, 2019, **15**, 323–334.
8 P. Kumar, M. C. Mathpal, S. Ghosh, G. K. Inwati, J. R. Maze, M.-M. Duvenhage, W. D. Roos and H. C. Swart, *J. Alloys Compd.*, 2022, **909**, 150026.
9 P. Kumar, G. K. Inwati, M. C. Mathpal, S. Ghosh, W. D. Roos and H. C. Swart, *Appl. Surf. Sci.*, 2021, **560**, 164789.
10 R. Rai, S. N. Gummadi and D. K. Chand, *ACS Omega*, 2019, **4**(27), 22514–22520.
11 N. Yehuda, Y. Turkulets, I. Shalish, A. Kushmaro and S. Malis Arad, *ACS Appl. Mater. Interfaces*, 2021, **13**(6), 7070–7079.
12 S. Behzadinasab, M. D. Williams, J. O. Falkinham Iii and W. A. Ducker, *J. Colloid Interface Sci.*, 2023, **652**, 1867–1877.
13 L. Mao, X. Zhao, Y. Xiao and G. Dong, *New J. Chem.*, 2019, **43**(10), 4196–4204.
14 Y.-H. Zhang, X.-L. Cai, D.-Y. Guo, H.-J. Zhang, N. Zhou, S.-M. Fang, J.-L. Chen and H.-L. Zhang, *J. Mater. Sci.: Mater. Electron.*, 2019, **30**(7), 7182–7193.
15 L. Martin, H. Martinez, D. Poinot, B. Pecquenard and F. Le Cras, *J. Phys. Chem. C*, 2013, **117**(9), 4421–4430.
16 M. C. Biesinger, L. W. M. Lau, A. R. Gerson and R. S. C. Smart, *Appl. Surf. Sci.*, 2010, **257**, 887–898.
17 P. Steiner, V. Kinsinger, I. Sander, B. Siegwart and S. Hüfner, *Z. Phys. B:Condens. Matter*, 1987, **67**, 497–502.
18 L. Sun, C. Peng, L. Kong, Y. Li and W. Feng, *Energy Environ. Mater.*, 2023, **6**, e12323.
19 S. Kumar, Bhawna, A. Gupta, R. Kumar, A. Bharti, A. Kumar and V. Kumar, *J. Phys. Chem. C*, 2023, **127**(15), 7095–7106.
20 D. Kumar, N. Jain, V. Jain and B. Rai, *Appl. Surf. Sci.*, 2020, **514**, 145905.
21 S. Gong, J. Chen, X. Wu, N. Han and Y. Chen, *Catal. Commun.*, 2018, **106**, 25–29.
22 S. Zhang, C. Zhang, M. Zhang, X. Liu and S. Xue, *J. Mol. Struct.*, 2023, **1290**, 135960.
23 D. V. Sivkov, O. V. Petrova, S. V. Nekipelov, A. S. Vinogradov, R. N. Skandakov, S. I. Isaenko, A. M. Ob'edkov, B. S. Kaverin, I. V. Vilkov, R. I. Korolev and V. N. Sivkov, *Nanomaterials*, 2021, **11**, 2993.
24 J. Zhang, M. S. Azam, C. Shi, J. Huang, B. Yan, Q. Liu and H. Zeng, *RSC Adv.*, 2015, **5**(41), 32272–32282.
25 Y.-J. Wang and K.-G. Zhou, *J. Cent. South Univ.*, 2012, **19**(8), 2125–2129.
26 G. Richner and G. Puxty, *Ind. Eng. Chem. Res.*, 2012, **51**(44), 14317–14324.
27 L. Schneider, Y. Dong, J. Haverinen, M. Jaakkola and U. Lassi, *Biomass Bioenergy*, 2016, **91**, 134–142.
28 M. Karabacak, Z. Cinar, M. Kurt, S. Sudha and N. Sundaraganesan, *Spectrochim. Acta, Part A*, 2012, **85**, 179–189.
29 L. Ostervold, R. Daneshpour, M. Facchinei, B. Tran, M. Wetherington, K. Alexopoulos, L. Greenlee and M. J. Janik, *ACS Appl. Mater. Interfaces*, 2023, **15**, 27878–27892.
30 R. T. Davison, E. L. Kuker and V. M. Dong, *Acc. Chem. Res.*, 2021, **54**, 1236–1250.
31 W. Yan, A. T. Poore, L. Yin, S. Carter, Y.-S. Ho, C. Wang, S. C. Yachuw, Y.-H. Cheng, J. A. Krause, M.-J. Cheng, S. Zhang, S. Tian and W. Liu, *J. Am. Chem. Soc.*, 2024, **146**, 15176–15185.
32 Y. Feng, P.-H. Lee, D. Wu, Z. Zhou, H. Li and K. Shih, *J. Hazard. Mater.*, 2017, **331**, 81–87.
33 X. Liu, Y. Zhai, Z. Xu, L. Liu, W. Ren, Y. Xie, C. Li, Y. Zhu and M. Xu, *Chem. Eng. J.*, 2023, **457**, 141106.